The Derivation of Absolute Potential Temperature Perturbations and Pressure Gradients from Wind Measurements in Three-Dimensional Space

YU-CHIENG LIOU

Department of Atmospheric Sciences, National Central University, Chung-Li, Taiwan

(Manuscript received 21 January 2000, in final form 2 June 2000)

ABSTRACT

A thermodynamic retrieval scheme has been developed by which one can derive the pressure and potential temperature perturbation fields from wind observations detected by remote sensing devices such as Doppler radar. In this method, the technique of variational analysis is applied to seek a set of optimal solutions for the pressure and potential temperature perturbations that, in the least squares sense, will simultaneously satisfy three momentum equations and the thermodynamic equation. The products of the retrieval are the three-dimensional absolute potential temperature fluctuations and the pressure perturbation gradients in any direction. Using artificial datasets generated by a numerical model, a series of experiments is conducted to test the proposed algorithm against various types of degraded input data. These primarily include finite difference approximations of the local temporal derivatives, random errors embedded in velocity observations with significant magnitudes, as well as incomplete data coverage. Improvements in the retrievals are found to be possible if, within a short period of time, wind data are available at multiple time levels. Overall, it has been demonstrated that the absolute potential temperature field and the pressure gradients can be determined with sufficient accuracy in a three-dimensional space. Such a capability is believed to be particularly useful in many meteorological applications.

1. Introduction

Doppler radar can provide information about radial wind with a high spatial and temporal resolution. Using the multiple-Doppler synthesis method (e.g., Armijo 1969; Ray et al., 1980), the structure of a complete three-dimensional wind field can be produced. More recently, the single Doppler wind retrieval technique, whereby one can recover unobserved cross-beam wind components using the reflectivities and the radial wind measurements obtained from a single Doppler radar, has been very successful. Details on this topic can be found in Sun et al. (1991), Qiu and Xu (1992), Laroche and Zawadzki (1994), Xu et al. (1994), Shapiro et al. (1995), Zhang and Gal-Chen (1996), and Liou (1999), among others. However, the structure of three-dimensional thermodynamic variables, such as temperature and pressure fluctuations, cannot be directly detected by radar. List and Lozowski (1970) have suggested, based on order-of-magnitude considerations, that these nonhydrostatic quantities are important. As a matter of fact, they are vital for a variety of meteorological purposes, ranging from the diagnostic studies of a mesoscale or storm-scale weather system to the initialization or data assimilation for a numerical weather prediction model. Therefore, the term ''thermodynamic retrieval,'' which represents a procedure whereby, from the wind measurements, the pressure and temperature perturbations can be inferred, has drawn much attention during the past two decades. Some early efforts at solving this problem can be found in a number of papers published in 1978. Bonesteele and Lin (1978), Hane and Scott (1978), Gal-Chen (1978), and Leise (1978) all reported on their own algorithms, which extracted the pressure or both the pressure and buoyancy from the velocity fields estimated either from real Doppler radar observations or the output of a numerical model simulation. Among these methods, the one proposed by Gal-Chen (1978) turned out to be particularly useful and was later widely adopted, sometimes being further modified by many researchers to deal with various situations [e.g., in Hane et al. (1981) for deep moist convection, in Gal-Chen and Kropfli (1984) for a precipitation-free planetary boundary layer observed during Project PHOENIX (1978), in Hane and Ray (1985) for a tornadic thunderstorm, in Lin et al. (1986) for convective cells within a squall line, and in Parsons et al. (1987) for a severe frontal rainband]. In addition, Roux et al. (1984) presented a similar method for analyzing the pressure and temperature fields within a West African squall line. Protat et al. (1998), on the other hand, have also described a new procedure for recovering thermodynamic

Corresponding author address: Dr. Yu-Chieng Liou, Department of Atmospheric Sciences, National Central University, Chung-Li, 320, Taiwan.
E-mail: tyliou@rainbow.atm.ncu.edu.tw

fields from Doppler radar data in order to study scale interactions.

Despite the encouraging results, it should be emphasized that in the retrieval algorithms described above only *deviations* (from the horizontal mean) in the pressure and temperature perturbations (with respect to a base state) are deduced for *each* layer. As a result, whenever an interpretation of the vertical structure of the thermodynamic fields is required one must proceed with caution. Unless some hypotheses, which may or may not be verifiable, are made, or independent field measurements of the temperature and pressure for each altitude are available, the absolute pressure and temperature fluctuations cannot be determined.

To overcome this difficulty, Brandes (1984) formulated a two-dimensional and a three-dimensional elliptic equation for the buoyancy and pressure perturbations, respectively. When solving for buoyancy, the pressure contributions were neglected, and the lateral boundary condition was specified to be zero, so that one could obtain a unique solution. This condition is, however, adequate only when the weather system is well restricted within the computation domain and the forcing is very weak along the boundaries. A major step forward was accomplished by Roux (1985, 1988). He proposed a different approach, whereby the pressure and temperature perturbations can be uniquely solved up to one constant. To deduce this unknown constant requires only one independent pressure and temperature observation at a single point somewhere in the retrieval domain. Applying Roux's results (1985, 1988) as boundary conditions, Sun and Roux (1988) were able to analyze the trailing anvil clouds of squall lines in a two-dimensional vertical cross section. Hauser et al. (1988) incorporated the variational procedure, as proposed by Roux (1985, 1988), into a retrieval system to derive both the thermodynamic and microphysical variables. Roux's scheme (1988) was further improved in Roux and Sun (1990) by their taking into account a simplified form of the thermodynamic equation everywhere in the domain, so that the value of the temperature gradient is provided in any direction. The validity of Roux and Sun (1990), however, was not fully investigated until Sun and Houze (1992) used the data from a simulated two-dimensional squall line with trailing stratiform precipitation. Additional improvements in Roux's retrieval technique can be found in Roux et al. (1993). With the rapid development of the adjoint method, Sun and Crook (1996) demonstrated the advantages of using the so-called 4D-Var technique over the traditional Gal-Chen (1978) scheme for retrieving the thermodynamic field. In contrast to the previous techniques, an important feature shown by the 4D-Var formulation is that the absolute temperature perturbations could be deduced without any independent measurements.

In this research a different approach is proposed. The basic methodology involves implementing the horizontal and vertical equations of motion and the thermodynamic equation into a single cost function. Through the method of variational analysis, a set of optimally determined potential temperature fluctuations and pressure perturbation gradients, which minimize this cost function, can be deduced simultaneously.

This paper is organized as follows. In the next section the proposed method is discussed in detail. Section 3 gives the datasets used for verification. Comparisons and discussions of the retrieval results are presented in section 4, followed by the conclusions in section 5.

2. Methodology

It is difficult to prepare a complete three-dimensional wind, temperature, and pressure field set from real field observations. Therefore, in order to fully investigate the performance and properties of this method, the validation is carried out using artificial datasets generated by a numerical model. To simplify the problem, the air is assumed to be dry. The basic momentum equations may be written in a fixed frame of reference as follows:

$$\frac{1}{\theta_0}\left[\frac{\partial u}{\partial t} + \mathbf{V}\cdot\nabla u - fv + \text{turb}(u)\right] = -\frac{\partial \pi'}{\partial x} \equiv -F, \quad (1)$$

$$\frac{1}{\theta_0}\left[\frac{\partial v}{\partial t} + \mathbf{V}\cdot\nabla v + fu + \text{turb}(v)\right] = -\frac{\partial \pi'}{\partial y} \equiv -G, \quad (2)$$

and

$$\frac{1}{\theta_0}\left[\frac{\partial w}{\partial t} + \mathbf{V}\cdot\nabla w + \text{turb}(w)\right] = -\frac{\partial \pi'}{\partial z} + g\frac{\theta'}{\theta_0^2} \equiv -H, \quad (3)$$

where the wind vector $\mathbf{V}$ has three Cartesian components (u, v, w), θ is the potential temperature, f refers to the Coriolis parameter, g stands for the gravity, and turb( ) denotes a subgrid-scale turbulence parameterization operator. The numerical model adopts a normalized form of pressure, called Exner function π, defined as

$$\pi = C_p\left(\frac{P}{P_0}\right)^{R/C_p}, \quad (4)$$

in which P is the pressure, $P_o = 100$ kPa, R is the gas constant, and C_p is the specific heat capacity at a constant pressure. Note that the subscript o represents a horizontally homogeneous basic state from which the nonhydrostatic perturbations are expressed by variables with a single prime. Since F, G, and H are functions of the winds only, their values can be estimated when the three-dimensional air motion is known through a procedure such as multiple-Doppler radar syntheses.

In addition to the momentum equations, the thermodynamic equation is also employed to provide information on the potential temperature gradients. This equation is expressed as

$$u\frac{\partial\theta'}{\partial x}+v\frac{\partial\theta'}{\partial y}+w\frac{\partial\theta'}{\partial z}+w\frac{d\theta_0}{dz}+S=0 \quad \text{and} \tag{5}$$

$$S=\frac{\partial\theta'}{\partial t}+\text{turb}(\theta')-\text{source/sink}. \tag{6}$$

Note that in Eq. (5), S represents the total effect of the local time rate of change, the diffusion, and the source sink of θ'. Gal-Chen (1982) suggested using the radar-observed radial velocity or reflectivities to define a moving frame of reference on which the global temporal evolution can be minimized. However, this concept is not applicable to Eq. (5), since in this case temperature is not an observable quantity. One can proceed with further parameterizations for the second and third terms on the right-hand side of Eq. (6), but this is not done here. Instead, S is treated as another unknown variable, and the experiments discussed later show that it can also be recovered.

From Eqs. (1)–(5), a cost function can be formulated:

$$J=\frac{1}{2}\int\int\int\int_{\Omega}(\alpha_1P_1^2+\alpha_2P_2^2+\alpha_3P_3^2+\alpha_4P_4^2+\alpha_5P_5^2+\alpha_6P_6^2+\alpha_7P_7^2+\alpha_8P_8^2)\,d\Omega, \tag{7}$$

where

$$d\Omega=dxdydzdt, \qquad P_1=\left(\frac{\partial\pi'}{\partial x}-F\right),$$

$$P_2=\left(\frac{\partial\pi'}{\partial y}-G\right), \qquad P_3=\left(\frac{\partial\pi'}{\partial z}-g\frac{\theta'}{\theta_0^2}-H\right),$$

$$P_4=\left(u\frac{\partial\theta'}{\partial x}+v\frac{\partial\theta'}{\partial y}+w\frac{\partial\theta'}{\partial z}+w\frac{d\theta_0}{dz}+S\right),$$

$$P_5=\left(\frac{\partial\theta'}{\partial z}\right), \qquad P_6=\frac{\partial^2\pi'}{\partial x^2}+\frac{\partial^2\pi'}{\partial y^2}+\frac{\partial^2\pi'}{\partial z^2},$$

$$P_7=\frac{\partial^2\theta'}{\partial x^2}+\frac{\partial^2\theta'}{\partial y^2}+\frac{\partial^2\theta'}{\partial z^2}, \quad \text{and}$$

$$P_8=\frac{\partial^2S}{\partial x^2}+\frac{\partial^2S}{\partial y^2}+\frac{\partial^2S}{\partial z^2}.$$

In Eq. (7), the first two terms (P_1^2, P_2^2) measure the distance between the retrieved horizontal pressure gradients and the calculated F and G (from the wind observations), respectively. The term P_3^2 denotes the difference in the retrieved vertical pressure gradient, the buoyancy, and the quantity H. Their weighting coefficients, α_1–α_3, are estimated by

$$\alpha_1=\left[\frac{1}{\Omega}\int\int\int\int_{\Omega}(F^2)\,d\Omega\right]^{-1},$$

$$\alpha_2=\left[\frac{1}{\Omega}\int\int\int\int_{\Omega}(G^2)\,d\Omega\right]^{-1}, \quad \text{and}$$

$$\alpha_3=\left[\frac{1}{\Omega}\int\int\int\int_{\Omega}(H^2)\,d\Omega\right]^{-1}. \tag{8}$$

The term P_4^2 represents the thermodynamic equation, which offers a constraint throughout the potential temperature field's spatial distributions. Its weighting coefficient α_4 is first defined as a function of the wind speed with the form

$$\alpha_4(V)=\frac{V^a}{V_0^b+V^b}, \tag{9}$$

where V_0 is a prescribed constant, and the wind speed V is

$$V=\sqrt{u^2+v^2+w^2}.$$

A simple calculation shows that when $b=2a$, the maximum for α_4 occurs at $V=V_0$, with the value $(2V_0^a)^{-1}$. In this work, we let $a=2$ and $V_0=1.5$ m s^{-1}. This coefficient is then normalized by its own maximum. Thus, the final form of α_4 becomes

$$\alpha_4(V)=\frac{1}{(2V_0^2)^{-1}}\left(\frac{V^2}{V_0^4+V^4}\right). \tag{10}$$

Equation (10) is designed so that when the solutions for the potential temperature fluctuations become unstable at points where the wind speed is too weak, the weighting coefficient would decrease accordingly. On the other hand, this coefficient also approaches zero when the advection effect is too strong to be handled properly in a fixed frame of reference.

The weighting coefficient α_5 is defined as

$$\alpha_5=\begin{cases}0.4, & \dfrac{\partial\theta'}{\partial z}<0\\ 0.0, & \dfrac{\partial\theta'}{\partial z}>0.\end{cases} \tag{11}$$

The role played by the constraint function, P_5^2, deserves some discussion. Our calculation indicates that within the retrieval domain, the ratio between the grid points, with $\partial\theta'/\partial z<0$ to $\partial\theta'/\partial z>0$, is approximately 1:8, which means that there are actually many points that are thermally unstable. In other words, $\partial\theta'/\partial z<0$ is

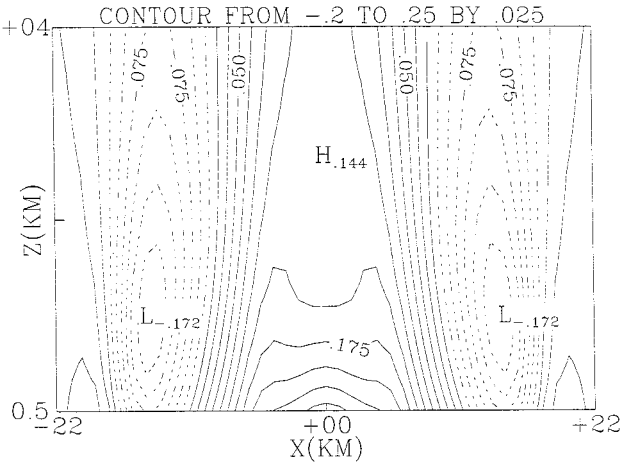

FIG. 1. "True" pressure field ($\pi' - \langle\pi'\rangle$, $\langle\,\rangle$ denotes a volume wide average) at the center cross section of the domain.

physically true. However, based on the experimental results (not shown), it can be seen that this constraint can effectively eliminate the "spurious" thermal instability, while the "true" thermally unstable region is kept intact. Note that P_5^2 is added as a "weak" constraint, so that with adequate weighting it would not force $\partial\theta'/\partial z < 0$ to disappear completely.

Although interpreted differently, this constraint is also included in the retrieval technique proposed by Roux and Sun (1990), as well as in the improved version suggested by Roux et al. (1993). Sun and Crook (1996) also adopted this constraint for the same purpose in their 4D-Var retrieval formulations. It should be pointed out that in the wide applications of the 3D- or 4D-Var techniques, it is not uncommon to introduce a constraint based on the outcome of the minimization. For example, in the work of single Doppler radar wind retrieval, the vertical vorticity ($\partial v/\partial x - \partial u/\partial y$) sometimes appears in the cost function as an extra penalty function. This weak vorticity constraint does produce better results, due to the reductions of ill conditioning and noise (e.g., Qiu and Xu 1996).

Finally, constraints P_6^2–P_8^2 are added as low-pass filters to suppress noise. Similar to Testud and Chong (1983), the weighting coefficients, α_6–α_8, are estimated by

$$\alpha_6 = \alpha_7 = \alpha_8 = \frac{\mu}{N} = \frac{k_0^{-4}}{N}, \tag{12}$$

where k_0 denotes the cutoff wavenumber, and N is the total number of grid points in the retrieval domain. If 2Δ is chosen as the cutoff wavelength, where Δ is the horizontal grid resolution then the corresponding value of μ equals $(\Delta/\pi)^4 \sim 0.01\Delta^4$. The usefulness of P_6^2–P_8^2 is further explained in section 4c.

From the first three cost function constraints, it is clear that the potential temperature appears in its *absolute* form, but the pressure is always expressed by first-order derivatives. Consequently, when Eq. (7) is minimized, the results will provide the structure of the buoyancy field in a three-dimensional space, as well as the pressure fluctuations gradients, not only for each horizontal plane but also in the vertical direction. In other words, the potential temperature field itself is determined, as is the pressure field up to a "volume wide" constant. We believe this to be an important advance over the traditional Gal-Chen (1978) scheme. When it is desirable to compare the retrieved absolute pressure perturbations against the true solutions, one should remove the average over the entire domain from each field, respectively.

Equation (7) is a functional with a very large number of dimensionalities. To minimize it, a quasi-Newtonian conjugate-gradient algorithm, named VA15AD by Liu and Nocedal (1988), is employed. This method requires the knowledge of the cost function gradients with respect to π', θ', and S at each point. Therefore, by applying variational analysis, one arrives at the following. For interior points,

$$\frac{\partial J}{\partial \pi'} = \int \left\{ -\left[\frac{\partial(\alpha_1 P_1)}{\partial x} + \frac{\partial(\alpha_2 P_2)}{\partial y} + \frac{\partial(\alpha_3 P_3)}{\partial z}\right] + \frac{\partial^2}{\partial x^2}\left(\alpha_6 \frac{\partial^2 \pi'}{\partial x^2}\right) + \frac{\partial^2}{\partial y^2}\left(\alpha_6 \frac{\partial^2 \pi'}{\partial y^2}\right) + \frac{\partial^2}{\partial z^2}\left(\alpha_6 \frac{\partial^2 \pi'}{\partial z^2}\right)\right\} dt, \tag{13}$$

$$\frac{\partial J}{\partial \theta'} = \int \left\{ -\left[\frac{\alpha_3 P_3 g}{\theta_0^2} + \frac{\partial(\alpha_4 P_4 u)}{\partial x} + \frac{\partial(\alpha_4 P_4 v)}{\partial y} + \frac{\partial(\alpha_4 P_4 w)}{\partial z} + \frac{\partial\left(\alpha_5 \dfrac{\partial \theta'}{\partial z}\right)}{\partial z}\right] + \left[\frac{\partial^2}{\partial x^2}\left(\alpha_7 \frac{\partial^2 \theta'}{\partial x^2}\right) + \frac{\partial^2}{\partial y^2}\left(\alpha_7 \frac{\partial^2 \theta'}{\partial y^2}\right) + \frac{\partial^2}{\partial z^2}\left(\alpha_7 \frac{\partial^2 \theta'}{\partial z^2}\right)\right]\right\} dt, \tag{14}$$

$$\frac{\partial J}{\partial S} = \int \left\{ \alpha_4 P_4 + \left[\frac{\partial^2}{\partial x^2}\left(\alpha_8 \frac{\partial^2 S}{\partial x^2}\right) + \frac{\partial^2}{\partial y^2}\left(\alpha_8 \frac{\partial^2 S}{\partial y^2}\right) + \frac{\partial^2}{\partial z^2}\left(\alpha_8 \frac{\partial^2 S}{\partial z^2}\right)\right]\right\} dt; \tag{15}$$

for $x = x_{\text{left}}$

$$\frac{\partial J}{\partial \pi'} = \int \left[-\alpha_1 P_1 + \frac{\partial}{\partial x}\left(\alpha_6 \frac{\partial^2 \pi'}{\partial x^2}\right)\right] dt,$$

$$\frac{\partial J}{\partial \theta'} = \int \left[-\alpha_4 u P_4 + \frac{\partial}{\partial x}\left(\alpha_7 \frac{\partial^2 \theta'}{\partial x^2}\right)\right] dt;$$

$$\frac{\partial J}{\partial S} = 0; \tag{16}$$

for $x = x_{\text{right}}$

$$\frac{\partial J}{\partial \pi'} = \int \left[\alpha_1 P_1 - \frac{\partial}{\partial x}\left(\alpha_6 \frac{\partial^2 \pi'}{\partial x^2}\right)\right] dt,$$

$$\frac{\partial J}{\partial \theta'} = \int \left[\alpha_4 u P_4 - \frac{\partial}{\partial x}\left(\alpha_7 \frac{\partial^2 \theta'}{\partial x^2}\right)\right] dt;$$

$$\frac{\partial J}{\partial S} = 0; \tag{17}$$

for $y = y_{\text{left}}$

$$\frac{\partial J}{\partial \pi'} = \int \left[-\alpha_2 P_2 + \frac{\partial}{\partial y}\left(\alpha_6 \frac{\partial^2 \pi'}{\partial y^2}\right)\right] dt,$$

$$\frac{\partial J}{\partial \theta'} = \int \left[-\alpha_4 v P_4 + \frac{\partial}{\partial y}\left(\alpha_7 \frac{\partial^2 \theta'}{\partial y^2}\right)\right] dt;$$

$$\frac{\partial J}{\partial S} = 0; \tag{18}$$

for $y = y_{\text{right}}$

$$\frac{\partial J}{\partial \pi'} = \int \left[\alpha_2 P_2 - \frac{\partial}{\partial y}\left(\alpha_6 \frac{\partial^2 \pi'}{\partial y^2}\right)\right] dt,$$

$$\frac{\partial J}{\partial \theta'} = \int \left[\alpha_4 v P_4 - \frac{\partial}{\partial y}\left(\alpha_7 \frac{\partial^2 \theta'}{\partial y^2}\right)\right] dt;$$

$$\frac{\partial J}{\partial S} = 0; \tag{19}$$

for $z = z_{\text{bottom}}$

$$\frac{\partial J}{\partial \pi'} = \int \left[-\alpha_3 P_3 + \frac{\partial}{\partial z}\left(\alpha_6 \frac{\partial^2 \pi'}{\partial z^2}\right)\right] dt,$$

$$\frac{\partial J}{\partial \theta'} = \int \left[-\left(\alpha_4 w P_4 + \alpha_5 \frac{\partial \theta'}{\partial z}\right) + \frac{\partial}{\partial z}\left(\alpha_7 \frac{\partial^2 \theta'}{\partial z^2}\right)\right] dt;$$

$$\frac{\partial J}{\partial S} = 0; \quad \text{and} \tag{20}$$

for $z = z_{\text{top}}$

$$\frac{\partial J}{\partial \pi'} = \int \left[\alpha_3 P_3 - \frac{\partial}{\partial z}\left(\alpha_6 \frac{\partial^2 \pi'}{\partial z^2}\right)\right] dt,$$

$$\frac{\partial J}{\partial \theta'} = \int \left[\alpha_4 w P_4 + \alpha_5 \frac{\partial \theta'}{\partial z} - \frac{\partial}{\partial z}\left(\alpha_7 \frac{\partial^2 \theta'}{\partial z^2}\right)\right] dt,$$

$$\frac{\partial J}{\partial S} = 0. \tag{21}$$

To avoid any inconsistency, the cost function in Eq. (7), as well as the expressions for the gradients shown in Eqs. (13)–(21), have to be coded in finite difference form, based upon the model's grid system (Sasaki et al. 1979). Then, using an initial zero guess for the unknown variables, and the gradients for J computed by Eqs. (13)–(21), subroutine VA15AD can find a new estimate of the solution. This process is iterated until a set of optimal pressure and potential temperature fluctuations is obtained, which makes the functional J reach a nearly steady state near the minimum.

The author would like to point out that all existing thermodynamic retrieval techniques start by using real Doppler radar wind data, in which errors are inevitable, to fit those terms in the momentum equations that are functions of the velocities only. The minimization methods used by Roux (1985, 1988) and Roux and Sun (1990) require further spatial derivatives of the momentum equations, and it is our speculation that this procedure might amplify the influence of the observational errors. By contrast, in this study, the momentum equations are directly applied in their original forms without any additional derivatives. Thus, the problem mentioned above can be avoided. However, this issue needs to be verified by a thorough comparison using real radar data.

3. Datasets and indices for verification

In this paper the datasets used for validation come from the numerical simulation of a collapsing cold pool, a frequently observed mesoscale phenomenon. The model domain contains a total of $55 \times 55 \times 55$ grid points. The horizontal and vertical resolutions are specified to be 1000 m and 150 m, respectively. Thus, the simulation is performed within three-dimensional space with a volume of approximately $55 \times 55 \times 8$ km^3. Assuming that the background atmosphere is neutral, with a basic state potential temperature of 300 K, the initial temperature perturbation is given by

$$\theta' = \begin{cases} d \le r_c, & 4.0\dfrac{e^{(d-r_c)/r_c} - e^{-(d-r_c)/r_c}}{e^{(d-r_c)/r_c} + e^{-(d-r_c)/r_c}} \\ d > r_c, & 0, \end{cases} \tag{22}$$

where d is the distance from the cold pool center, and r_c represents the radius of the cold pool and is set to be 10 km. The model is integrated in time for 30 min. No perturbations are given in the initial pressure field. The

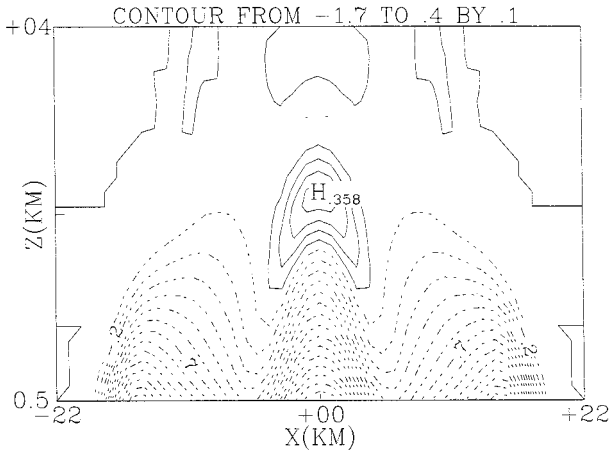

FIG. 2. ''True'' potential temperature perturbation (θ') field at the center cross section of the domain.

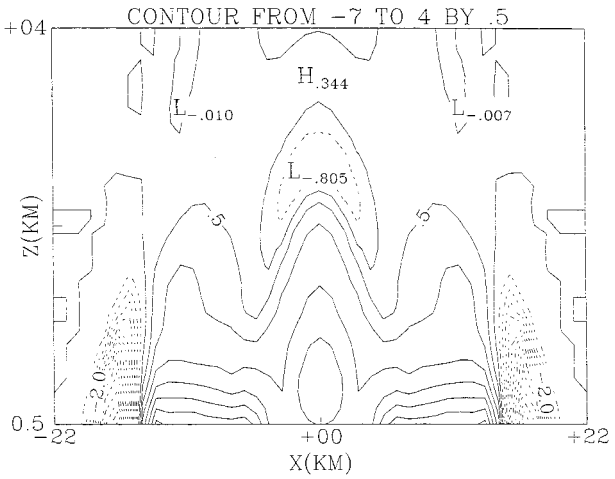

FIG. 3. ''True'' S field at the center cross section of the domain. The contours are amplified by 10^3. See text for the definition of S.

dimension of the domain as well as the size and strength of the initial perturbations are cautiously specified so that when relevant variables are extracted during the simulation, the fully developed flow will remain well inside the simulation domain. Figures 1 and 2 show the simulated pressure and potential temperature perturbations on a vertical x–z cross section passing through the center of the cold pool after 20 min of simulation time. Note that in Fig. 1 the volume average has been removed. The residue term (S) discussed in Eqs. (5) and (6) is also illustrated in Fig. 3, using the model outputs. These three fields are selected as true solutions for verifying the retrieval results.

To investigate the accuracy of the retrieval results, several indices are evaluated. If A represents either the potential temperature or the pressure, and the subscripts t or r denote the ''true'' or ''retrieved'' quantities, respectively, we then obtain the following definitions: root-mean-squared errors (rmse's),

$$\sqrt{\frac{1}{N}\sum (A_r - A_t)^2}; \tag{23}$$

spatial correlation coefficient (SCC),

$$\mathrm{SCC}(A) = \frac{\sum (A_r - \overline{A}_r)(A_t - \overline{A}_t)}{\sqrt{\sum (A_r - \overline{A}_r)^2 \sum (A_t - \overline{A}_t)^2}},$$

$$\overline{A} = \frac{1}{N}\sum A. \tag{24}$$

Here, $\overline{A}$ can be an average taken over a three-dimensional volume or a two-dimensional plane. The term N is the total number of grid points in the volume/plane. Reliability parameter for retrievals (E_r):

$$E_r \equiv \frac{\iiint \left[\left(\frac{\partial \pi_r'}{\partial x} - F\right)^2 + \left(\frac{\partial \pi_r'}{\partial y} - G\right)^2 + \left(\frac{\partial \pi_r'}{\partial z} - \frac{\partial \pi_t'}{\partial z}\right)^2 + \left(g\frac{\theta_r'}{\theta_0^2} - g\frac{\theta_t'}{\theta_0^2}\right)^2\right] dx\, dy\, dz}{\iiint \left[F^2 + G^2 + \left(\frac{\partial \pi_t'}{\partial z}\right)^2 + \left(g\frac{\theta_t'}{\theta_0^2}\right)^2\right] dx\, dy\, dz}. \tag{25}$$

The SCC score measures the ''similarity'' between two fields. It reaches 1 when they are identical. The reliability parameter is analogous to the ''momentum-checking'' parameter by Gal-Chen and Kropfli (1984). They gave a threshold of 0.5, above which the retrieval is virtually meaningless. Hane and Ray (1985) also suggested that an $E_r \leq 0.25$ would be considered to be a good fit.

4. Experimental design and results

The experiments and brief descriptions are listed in Table 1. To reduce the influence from the numerical model's boundary conditions, most of the retrieval experiments were conducted within a smaller domain, with $45 \times 45 \times 33$ grid points, except for case 12. Basically, the experiments are conducted to investigate the fea-

TABLE 1. Summary of experimental design.

Case	Description
1	Control run used to investigate the applicability of the proposed formulation.
2	Testing the sensitivity to the length of the time interval between two sets of Doppler wind observations.
3	Only momentum equations (P_1^2–P_3^2) are used as constraints.
4	Demonstrating the usefulness of the low-pass filter constraints (P_6^2–P_8^2).
5	Testing the performance of the a posteriori filter.
6	Testing the performance of the a priori filter.
7	Testing the tolerance of the complete cost function, equipped by penalty functions, against observational errors.
8	Same as in 7, but with larger random errors.
9	Testing the performance using data from multiple time levels.
10	*F* and *G* are randomly perturbed, but *H* is not.
11	*H* is randomly perturbed, but *F* and *G* are not.
12	Sensitivity test for incomplete data coverage. Retrieval domain is 31 × 31 × 18 and 45 × 45 × 10.

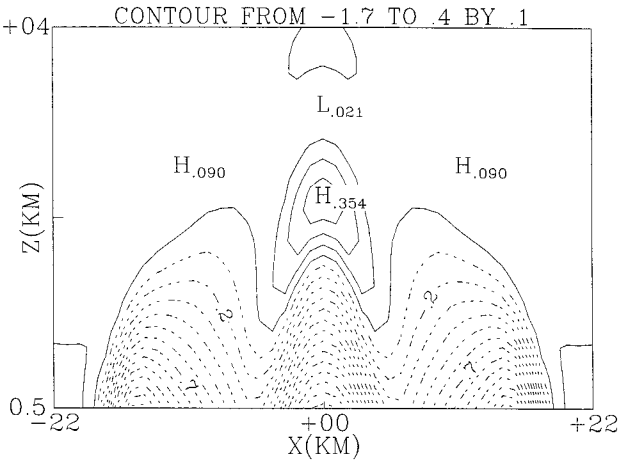

FIG. 5. Same as in Fig. 2 but for case 1, the control run.

sibility of the proposed formulation as well as its sensitivity to various types of degraded input data. We will now focus on the vertical structure of the retrieved thermodynamic variables.

a. Control run

It is known, from Eqs. (1)–(3), that the input data for all the experiments are *F*, *G*, and *H*, which, in real situations, can be completely determined using the wind observations. However, to examine the performance of the proposed method, the input data should be as accurate as possible. The best way to achieve this is to directly use the model-generated pressure and the potential temperature perturbations. Using this approach, case 1 represents a control run in which a set of *F*, *G*, and *H* is constructed using the model outputs from π' and θ' at $T = 20$ min. This is then substituted into the retrieval algorithm without contamination. It should be pointed out that even with perfect input data, one should not expect an exact solution from the proposed scheme. This is because the strategy as outlined in section 2 only iteratively seeks an approximated solution, which will minimize the distance between the model equations and the data. By contrast, the traditional methods, such as Gal-Chen (1978), directly solve for the exact thermodynamic variables from the model equations. With this in mind, Figs. 4–6 illustrate the retrieved fields. Their degree of agreement to the true solutions (Figs. 1–3) is obvious. The consistency between the true and the retrieved residue term (*S*) is especially encouraging. Since this variable represents the total effects of the local temporal change, turbulence, and source/sink, one can perform further parameterizations to separate each term's contribution.

To make a quantitative comparison, the indices introduced in Eqs. (23)–(25) are calculated globally over the whole retrieval domain. Table 2 shows the resulting statistics. The value of E_r ($=0.819 \times 10^{-1}$) is far below 0.25, indicating a successful retrieval. Of particular sat-

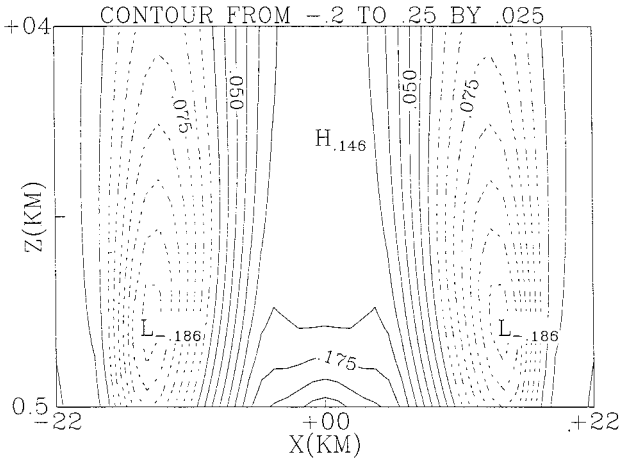

FIG. 4. Same as in Fig. 1 but for case 1, the control run.

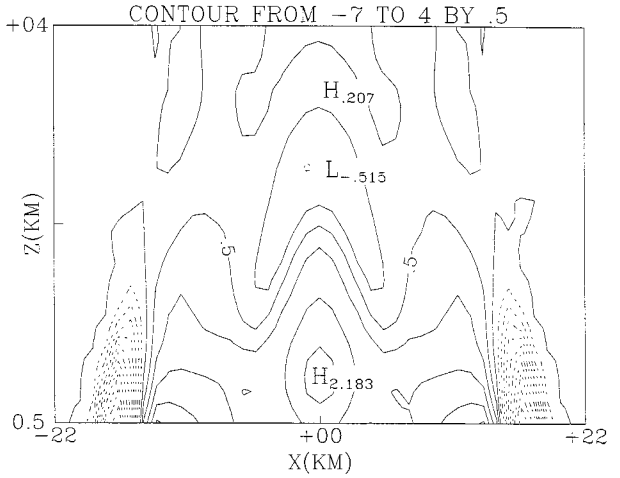

FIG. 6. Same as in Fig. 3 but for case 1, the control run.

TABLE 2. Statistical results for cases 1–2.

Case	Comments	rmse			SCC			E_r
		P' (mb)	θ' (K)	S (K/s)	π'	θ'	S	
1	Control Run	0.323×10^{-1}	0.903×10^{-1}	0.114×10^{-3}	0.983	0.999	0.993	0.819×10^{-1}
2	Δt = 12 s	0.332×10^{-1}	0.933×10^{-1}	0.873×10^{-4}	0.983	0.996	0.996	0.871×10^{-1}
2	Δt = 60 s	0.326×10^{-1}	0.946×10^{-1}	0.176×10^{-3}	0.983	0.994	0.977	0.890×10^{-1}
2	Δt = 180 s	0.334×10^{-1}	0.103	0.446×10^{-3}	0.982	0.981	0.847	0.104
2	Δt = 300 s	0.456×10^{-1}	0.151	0.814×10^{-3}	0.971	0.894	0.656	0.214

isfaction are the good SCC scores for all three retrieved variables, which imply a close similarity between the retrieved and the true fields in three-dimensional space. Since this study emphasizes the interpretation of the vertical structures, the SCC indices are computed again for each x–z cross section. Figure 7 displays the results layer by layer along the y coordinate, and one immediately recognizes that the high scores in the cold pool region ensure that the vertical structures of thermodynamic perturbations can be determined without ambiguity.

b. Data acquisition frequency

In case 2 the sensitivity of this retrieval scheme to the time intervals between each wind observation is explored. As discussed in Gal-Chen (1978), taking the time derivatives over a long interval is equivalent to simulating errors due to nonsimultaneous radar observations. To prepare the input data F, G, and H, the tendency terms (i.e., $\partial u/\partial t$, $\partial v/\partial t$, $\partial w/\partial t$) are calculated by finite differencing the model outputs of the velocity fields at T = 20 min − $\Delta t/2$ and T = 20 min + $\Delta t/2$. For the advection, Coriolis force, and turbulence parameterizations, we use the model results at T = 20 min. Before going into the experiments, a further examination of the numerical simulation reveals that at T = 20 min, the cold pool is still in the rapid development stage, propagating outward at a speed of about 10 m s^{-1}. To calculate the tendencies correctly, Gal-Chen (1979) suggested that the criterion for an allowable radar scan time Δt be defined as

$$\frac{U\Delta t}{L} = O(1), \tag{26}$$

where U is a typical velocity and L stands for the spatial resolution. In this study, L = 1000 m, and for $U \sim 10$ m s^{-1}, we have $\Delta t \sim 100$ s. Thus, in this experiment, the value of Δt is gradually increased from 12 s ($\ll$100 s, the length of one model time step) to 60 s ($<$100 s), then 180 s ($>$100 s), and finally 300 s ($\gg$100 s).

From Table 2, it is obvious that the proposed method works very well as Δt increases from 12 to 60 s. When Δt exceeds 100 s and reaches 180 s, the retrievals are still considered good, with E_r = 0.104, shown by the graphic results in Figs. 8 and 9. However, when Δt increases to 300 s, one finds that the increases of rmse, and the drops in SCC scores (especially for θ' and S) are substantial. The value of E_r (=0.214) is now near the 0.25 threshold. Of course, this is not surprising since Δt is already too long, compared to the criteria suggested in Eq. (26). Therefore, case 2 simply states that this retrieval algorithm does have a certain error tolerance introduced by the discreteness of the radar measurements. However, an intensive scanning strategy would be beneficial in terms of improving the quality of the retrievals. The author would like to point out that some

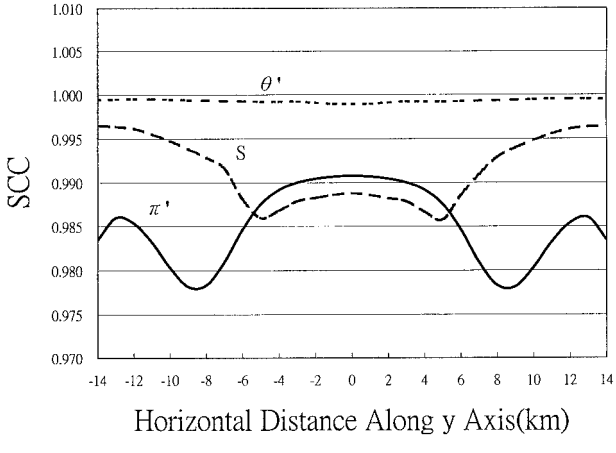

FIG. 7. The SCC score on each x–z cross section along the y coordinate for case 1. Solid line: π'; dashed line: θ'; long dashed line: residue term S.

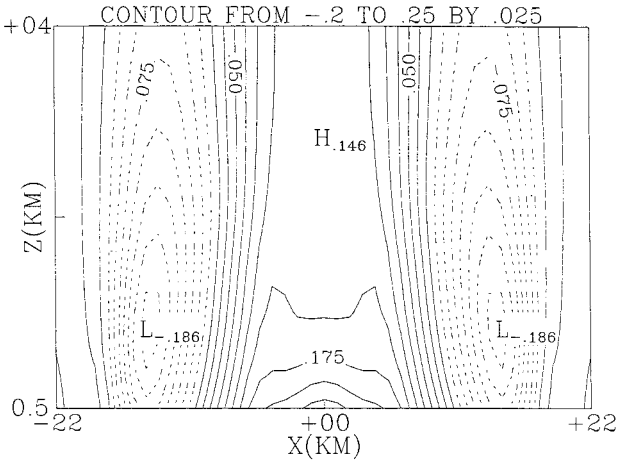

FIG. 8. Same as in Fig. 1 but for case 2, Δt = 180 s.

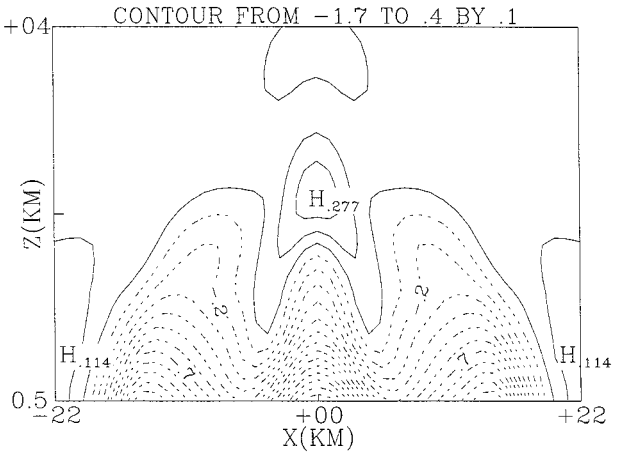

FIG. 9. Same as in Fig. 2 but for case 2, $\Delta t = 180$ s.

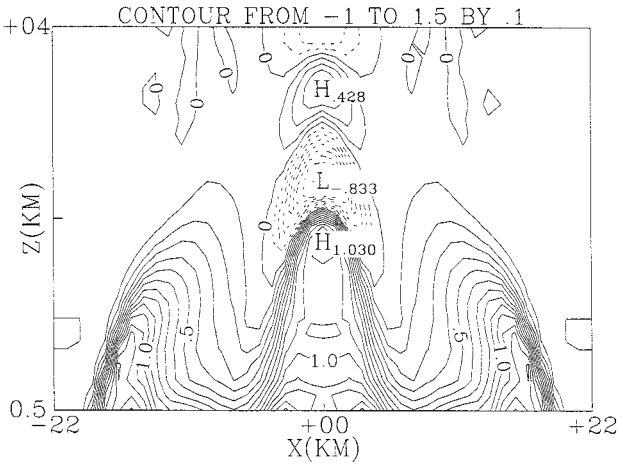

FIG. 10. "True" $\partial\theta'/\partial z$ field from model outputs. The contours are amplified by 10^3.

radars can perform very fast scans. For example, Wurman (1999) reported that the Doppler On Wheel system, equipped by new software/hardware developed for the National Center for Atmospheric Research S-band Dual Polarization Doppler radar was able to obtain a scanning rate of 30–50° s^{-1}, resulting in sector scans updates in 6–7 s, and volumetric updates in 30–50 s.

It may also be noted that in this experiment the pressure SCC score remains high (0.97–0.99) for different Δt, which implies, at least qualitatively, that the retrieved pressure perturbation field is robust for this kind of degraded data. By contrast, the SCC score of the residue term (S) decreases significantly from 0.9 to 0.6. We believe that this is because the residue term only appears once in the cost function Eq. (7). In other words, the lack of restrictions makes this quantity the most difficult one to be recovered. When observational errors are present, it is expected that only the rough pattern of the residues can be deduced.

c. *Insufficient constraints*

Mathematically, it is possible to use three constraints, P_1^2, P_2^2 and P_3^2, to solve for two unknowns, π' and θ'. But in case 3, when only these three constraints are employed in the cost function, it is found that the quality of the retrieved potential temperature deteriorates seriously, where the rmse of θ' reaches 0.156 K, the SCC index of θ' drops to 0.83, and the reliability parameter E_r rises to 0.23. It can be seen that in the cost function in Eq. (7), P_3^2 is different from the other terms since it contains both unknown variables (π' and θ'), and this particular constraint only requires that the difference between the vertical pressure gradient and the buoyancy be as close to H as possible, rather than individually imposing restrictions confining the pressure or the potential temperature. Under this condition, it seems possible that after the minimization procedure is completed, both the retrieved vertical pressure gradient and the buoyancy may share a common but unknown constant. When one calculates H, the buoyancy is subtracted from the vertical pressure gradient; therefore, this constant would be cancelled out. As a result, the difference between the vertical pressure gradient and the buoyancy may still be close to H, as required by the constraint, but the thermodynamic perturbations are poorly recovered. This experiment leads us to ponder the necessity of including more penalty functions. Fortunately, the previous control run demonstrates that, by adding more constraints, the possibility of obtaining this spurious constant can be effectively reduced.

Case 4 is used to investigate the usefulness of the smoothness penalty functions. The control run is repeated again, but with constraints P_6^2–P_8^2 turned off. Figures 10–12 display the vertical structure of $\partial\theta'/\partial z$, from the true solution, as well as its retrieved counterparts, with (control run) and without (case 4) the smoothness functions. By comparing the figures one may easily realize that these constraints can work effectively as low-pass filters to suppress noise. Note that these functions

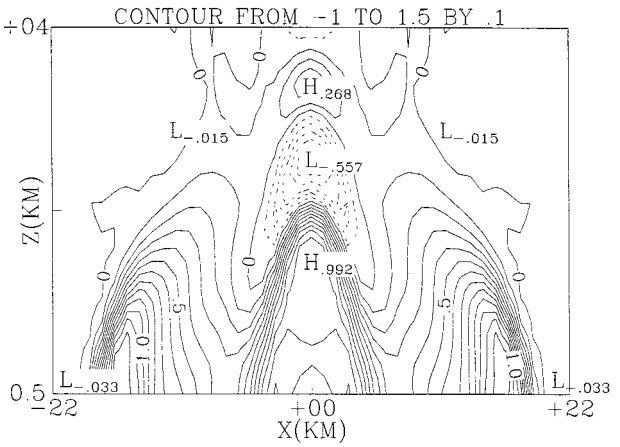

FIG. 11. Retrieved $\partial\theta'/\partial z$ field *with* smoothness penalty functions for case 1.

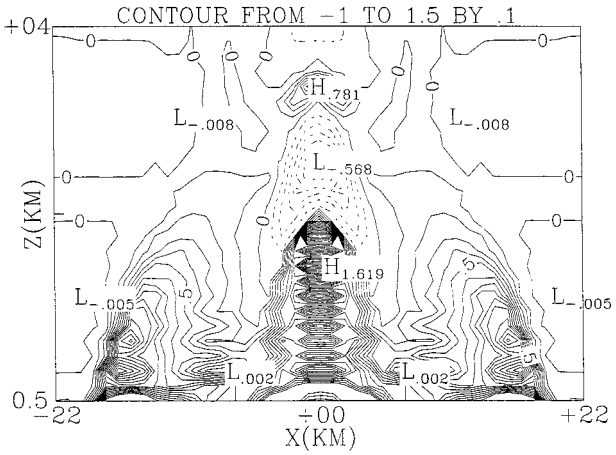

FIG. 12. Retrieved $\partial\theta'/\partial z$ field *without* smoothness penalty functions for case 4.

only appear in the cost function in the form of weak constraints. Therefore, with proper weighting, one should not worry about the complete elimination of the higher-order derivatives.

d. Imperfect input datasets

Cases 5–7 are devoted to studying the impact of using imperfect datasets, which can be ''imitated'' by superimposing random errors of varying magnitudes onto *F*, *G*, and *H*. To reduce the noise, filtering can be employed either on the input data (a priori) or on the resulting thermodynamic fields (a posteriori). The latter was advocated by Gal-Chen (1978) since he argued that filtering the input data would remove not only the noise but useful signals as well. Therefore, he suggested applying the filtering only to the results, not the input. Hane et al. (1981) adopted this procedure. However, a somewhat different conclusion was addressed by Gal-Chen and Kropfli (1984), where the traditional retrieval algorithm of Gal-Chen (1978) was applied to a real boundary layer case study (PHOENIX project 1978). To clarify this issue in our scheme, we compare the retrieved outputs from both procedures. To prepare the input datasets, let *A* represent either the *F*, or *G*, or *H* field at each grid point when $T = 20$ min; it is then altered by

$$A'(i, j, k) = A(i, j, k) + \varepsilon \times (2 \times \text{rdn} - 1) \times A(i, j, k), \quad (27)$$

where rdn denotes a random number generator, whose range is from 0 to 1, and ε specifies the maximum magnitude of the perturbations. Then, the perturbed field (A') is smoothed by a three-dimensional filter that has the following form:

$$\overline{A}(i, j, k) = \sum_{l=-1}^{1} \sum_{m=-1}^{1} \sum_{n=-1}^{1} \text{wt}(i + l, j + m, k + n) \times A'(i + l, j + m, k + n), \quad (28)$$

where wt is the weight assigned to the points around (i, j, k). Overall, 27 points are involved in smoothing the quantity at each grid point. If $S = |l| + |m| + |n|$, then when $S = 3$ (8 points), wt = 1/64; when $S = 2$ (12 points), wt = 1/32; when $S = 1$ (6 point), wt = 1/16; and when $S = 0$ (the center point), wt = 1/8. To isolate the influence of Eq. (27), we then temporarily turn off the smoothness penalty functions, P_6^2–P_8^2, in Eq. (7).

Let the maximum magnitude of the random error (ε) be 20% of the value at each point. Table 3 compares the statistics produced from the two types of filtering. In case 5, the a posteriori filter is utilized. The value of E_r (=0.733) is found to exceed the threshold value of 0.5, which, unfortunately, implies a failure. However, when the a priori filter is adopted in case 6, E_r decreases dramatically to 0.172. Other statistics also confirm that the a priori filter outperforms the a posteriori filter in every aspect. In addition, when the complete form of Eq. (7) is applied (case 7), Table 3 clearly reveals steady improvements in the retrievals when the type of smoothing is upgraded from an a posteriori filter (case 5) to an a priori filter (case 6), and then to an a priori filter + smoothness constraints P_6^2–P_8^2 (case 7). Similar to the conclusion reached in section 4c, in these experiments the SCC score for pressure varies only from 0.95 to 0.98, which again shows little dependence on the filters. Finally, Fig. 13 displays the vertical structure of the retrieved potential temperature fluctuations for case 7.

e. Multiple time levels

Case 8 is the same as case 7, but the maximum amplitude of the random error (ε) is specified by a much

TABLE 3. Statistical results for cases 5–7 and 10–11.

Case	Comments	rmse		SCC		
		P' (mb)	θ' (K)	π'	θ'	E_r
5	a posteriori filter	0.545×10^{-1}	0.262	0.950	0.886	0.733
6	a priori filter	0.340×10^{-1}	0.123	0.977	0.962	0.172
7	a priori + smoothness filter	0.327×10^{-1}	0.933×10^{-1}	0.981	0.995	0.985×10^{-1}
10	35% random errors to *F* and *G*	0.334×10^{-1}	0.109	0.979	0.976	0.136
11	35% random errors to *H*	0.329×10^{-1}	0.923×10^{-1}	0.982	0.997	0.914×10^{-1}

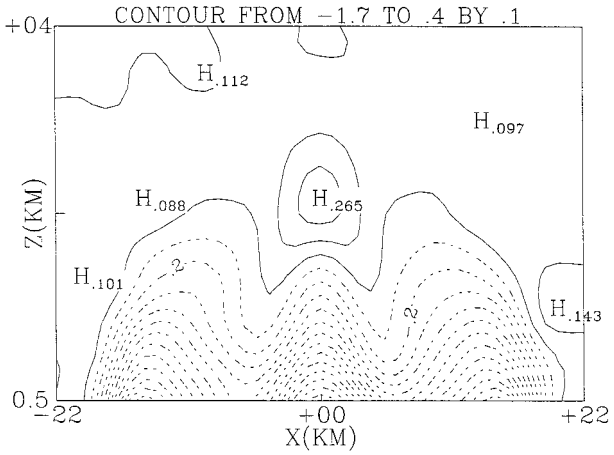

FIG. 13. Same as in Fig. 2 but for case 7, with randomly perturbed input data.

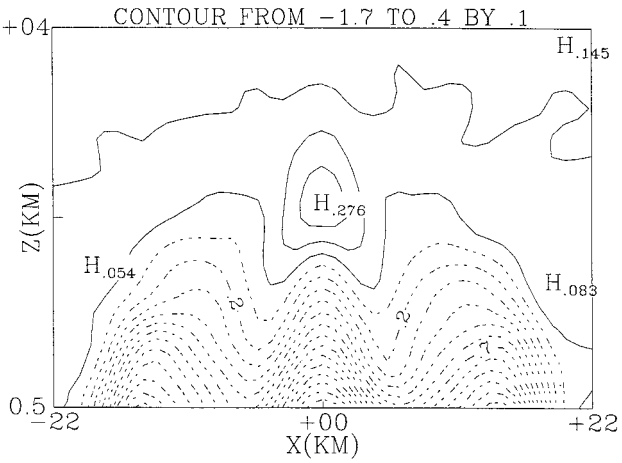

FIG. 15. Same as in Fig. 2 but for case 9, with input data from multiple time levels.

larger value, 0.35, to perturb the input datasets *F*, *G*, and *H* at T = 20 min. Then, in case 9, a different design is attempted in which *F*, *G*, and *H*, at three time levels (18.5, 20.0, and 21.5 min), are stored as input data. For a given point, this is equivalent to tripling the number of equations employed to find the optimal pressure and the potential temperature. Thus, the degree of ill-conditionness can be reduced. The resulting statistics do reveal additional improvements as the value of E_r decreases from 0.207 in case 8 (single time level) to 0.138 in case 9 (multiple time levels). Visual comparisons against the true solutions are made by showing the derived pressure and the potential temperature perturbation fields in Figs. 14 and 15, respectively. This demonstrates that if a Doppler radar can execute an intensive scanning mode, the use of data at multiple time levels offers more advantages in suppressing the impact of the noise.

f. Partially perturbed input data

The accuracy of the thermodynamic retrieval scheme depends on the quality of the wind measurements. It is known that the vertical velocities are prone to observational errors. To overcome this difficulty, a number of techniques have been developed (e.g., Ray et al. 1980; Gal-Chen and Kropfli 1984). Nevertheless, the vertical velocity field is still considered to be less reliable than its horizontal counterparts. As a result, the estimation of *H* is likely to be more sensitive to observational errors than *F* and *G*. Thus, it is of interest to examine the impact of *F*, *G* being contaminated differently than *H*. First, in case 10, we distort *F* and *G* by random errors, according to Eq. (27), while *H* is intact. Then, in case 11, only *H* is perturbed. In both cases, the magnitude of ε is set to be 0.35. Table 3 lists the statistical results, while the graphic results of the potential temperature fluctuations for these two experiments are presented in Figs. 16 and 17, respectively. In both cases, the principal

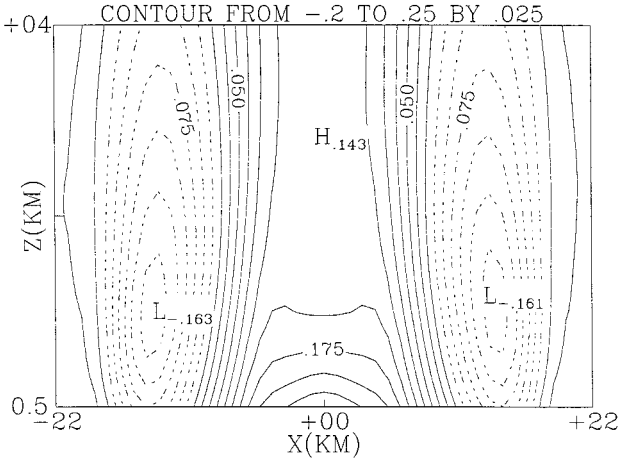

FIG. 14. Same as in Fig. 1 but for case 9, with input data from multiple time levels.

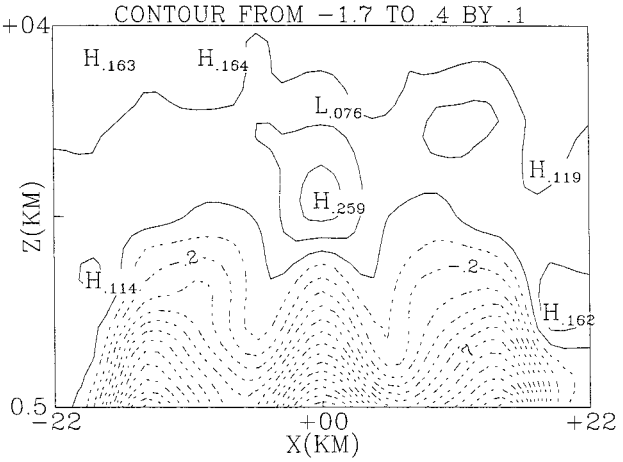

FIG. 16. Same as in Fig. 2 but for case 10 (*F*, *G* perturbed; *H* intact).

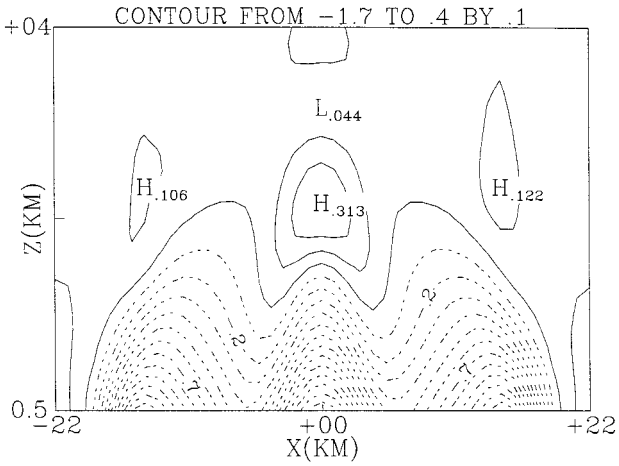

FIG. 17. Same as in Fig. 2 but for case 11 (*F*, *G* intact; *H* perturbed).

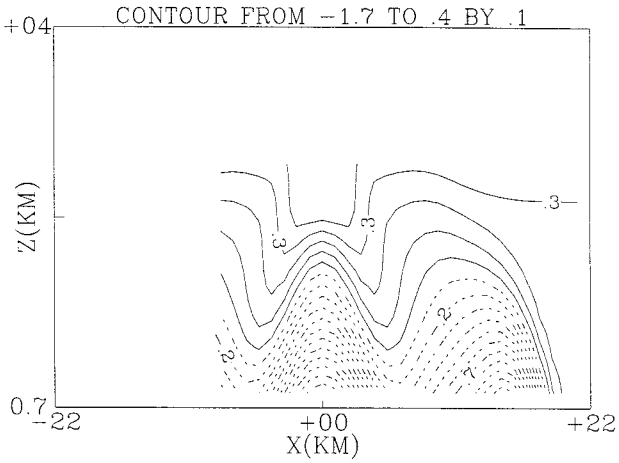

FIG. 18. Same as in Fig. 2 but for case 12 (domain size is 31 × 31 × 18).

features of the perturbations have been successfully recovered. However, further comparisons show the retrievals of case 11, with $E_r = 0.914 \times 10^{-1}$, are generally better than those of case 10, whose $E_r = 0.136$. Apparently, when *F* and *G* are accurate enough, the negative impact of the noise level in the *H* component can be effectively mitigated. It is also worth mentioning at this time that, in all the cases discussed above, one always obtains high SCC scores (>0.90) for pressure perturbations. This implies that the retrieved pressure is less influenced by observational errors than the potential temperature. This may be attributed to the constraints, P_1^2 and P_2^2, in Eq. (7), since they are adopted directly from the equations of motion and carry strong restrictions for confining the structure of a single unknown variable π'. It is believed that such a property will be of particular usefulness in many diagnostic studies of meteorological phenomena.

g. Incomplete data coverage

Case 12 is designed for the following scenario: the horizontal or vertical extent of the domain, where the observational data are available, is shortened. Then, how would the retrieval scheme respond to this incomplete data coverage? In this experiment the total number of grid points at which the wind measurements can be specified is decreased from 45 × 45 × 33 to 31 × 31 × 18, and to a much shallower region of 45 × 45 × 10. Compared to the size of the original domain, this is equivalent to an approximately 70% reduction. In the 31 × 31 × 18 run, we deliberately shift the smaller retrieval domain from the center of the cold pool so that the lateral boundary conditions would differ from one side to the other. Only the graphic results are presented in Figs. 18 and 19 for the derived potential temperature perturbations. It is very encouraging to see that the principal features within this particular region can still be successfully recovered with only slight distortions.

5. Conclusions and future work

In this research we proposed a different thermodynamic retrieval scheme for extracting the pressure and potential temperature field information from wind observations. Based on the aforementioned results, the following is a list of the conclusions.

- Numerical experiments have shown that the algorithm outlined in this research is a feasible tool to perform thermodynamic retrievals with sufficient accuracy.
- When the weather system of interest is evolving rapidly, the proposed method can tolerate, to some extent, the errors introduced by using finite differences to approximate the local temporal derivatives.
- Equipped with an a priori type of filter and smoothness penalty constraints, the proposed procedure can still extract meaningful results from seriously contaminated input datasets. Additional improvements are

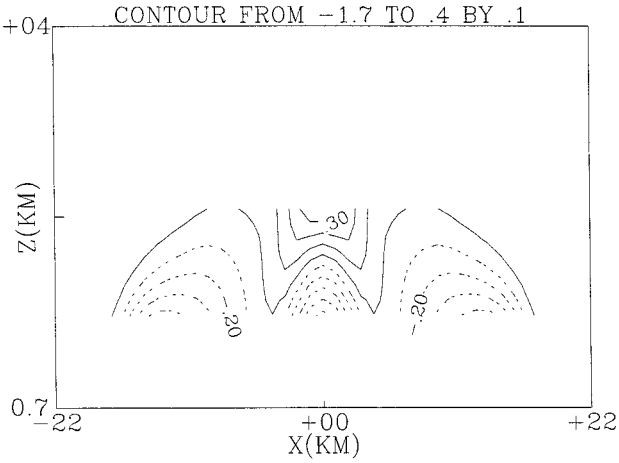

FIG. 19. Same as in Fig. 2 but for case 12 (domain size is 45 × 45 × 10).

possible, if wind measurements at multiple time levels are available.
- The influence introduced by errors in H component to the retrievals can be mitigated through accurately measured F and G components.
- At least in the qualitative sense, the pressure retrieval is quite robust for all types of degraded data.
- The retrieval scheme works well when input data coverage is incomplete.
- The products of the proposed scheme are the three-dimensional potential temperature fluctuations, and the pressure perturbation gradients, in any direction. Therefore, the interpretation of the pressure, or the potential temperature distributions in the vertical direction should no longer cause confusion. We believe that this is one advantage over the traditional scheme and is of particular usefulness in many meteorological applications.

The current study focuses on a simulated dry collapsing cold pool. Future work, some already underway, should include more testing using real Doppler radar observations and extend the method to incorporate microphysical variables.

Acknowledgments. The discussions with Prof. Tai-Chi Chen were highly appreciated. The author also wants to thank her for her encouragement during this study. This work is sponsored by the National Science Council of Taiwan, Republic of China, under Grants NSC 88-2111-M-008-027-A10 and NSC 89-2111-M-008-012-A10.

REFERENCES

Armijo, L., 1969: A theory for the determination of wind and precipitation velocities with Doppler radars. *J. Atmos. Sci.,* **26,** 570–573.

Bonesteele, R. G., and Y. J. Lin, 1978: A study of updraft-downdraft interaction based on perturbation pressure and single-Doppler radar data. *Mon. Wea. Rev.,* **106,** 62–68.

Brandes, E. A., 1984: Relationships between radar-derived thermodynamic variables and tornadogenesis. *Mon. Wea. Rev.,* **112,** 1033–1052.

Gal-Chen, T., 1978: A method for the initialization of the anelastic equations: Implications for matching models with observations. *Mon. Wea. Rev.,* **106,** 587–606.

——, 1979: A method for calculating temperature, pressure and vertical velocities from Doppler radar observations. Preprints, *Ninth Severe Storms Conf.,* Kansas City, KS, Amer. Meteor. Soc., 492–496.

——, 1982: Errors in fixed and moving frame of reference: Application for conventional and Doppler radar analysis. *J. Atmos. Sci.,* **39,** 2279–2300.

——, and R. A. Kropfli, 1984: Buoyancy and pressure perturbations derived from Dual-Doppler radar observations of the planetary boundary layer: Applications for matching models with observations. *J. Atmos. Sci.,* **41,** 3007–3020.

Hane, C. E., and B. C. Scott, 1978: Temperature and pressure perturbations within convective clouds derived from detailed air motion information: Preliminary testing. *Mon. Wea. Rev.,* **106,** 654–661.

——, and P. S. Ray, 1985: Pressure and buoyancy fields derived from Doppler radar data in a tornadic thunderstorm. *J. Atmos. Sci.,* **42,** 18–35.

——, R. B. Wilhelmson, and T. Gal-Chen, 1981: Retrieval of thermodynamic variables within deep convective clouds: Experiments in three dimensions. *Mon. Wea. Rev.,* **109,** 564–576.

Hauser, D., F. Roux, and P. Amayenc, 1988: Comparison of two methods for the retrieval of thermodynamic and microphysical variables from Doppler radar measurements: Application to the case of a tropical squall line. *J. Atmos. Sci.,* **45,** 1285–1303.

Laroche, S., and I. Zawadzki, 1994: A variational analysis method for retrieval of three-dimensional wind field from single-Doppler radar data. *J. Atmos. Sci.,* **51,** 2664–2682.

Leise, J. A., 1978: Temperature retrieval from dual-Doppler radar wind field data. Preprints, *18th Conf. On Radar Meteorology,* Atlanta, GA, Amer. Meteor. Soc., 94–99.

Lin, Y. J., T. C. Wang, and J. H. Lin, 1986: Pressure and temperature perturbations within a squall-line thunderstorm derived from SESAME dual-Doppler data. *J. Atmos. Sci.,* **43,** 2302–2327.

Liou, Y.-C., 1999: Single radar recovery of cross-beam wind components using a modified moving-frame of reference technique. *J. Atmos. Oceanic Technol.,* **16,** 1003–1016.

List, R., and E. P. Lozowski, 1970: Pressure perturbations and buoyancy in convective clouds. *J. Atmos. Sci.,* **27,** 168–170.

Liu, D. C., and J. Nocedal, 1988: On the limited memory BFGS method for large scale optimization. Tech. Rep. NAM 03, Department of Electric Engineering and Computer Science, Northwestern University, 26 pp. [Available from Department of Electric Engineering and Computer Science, Northwestern University, Evanston, IL 60208.]

Parsons, D. B., C. G. Mohr, and T. Gal-Chen, 1987: A severe frontal rainband. Part III: Derived thermodynamic structure. *J. Atmos. Sci.,* **44,** 1615–1631.

Protat, A., Y. Lemaitre, and G. Scialom, 1998: Thermodynamic analytic fields from Doppler-radar by means of the MANDOP analysis. *Quart. J. Roy. Meteor. Soc.,* **124,** 1633–1668.

Qiu, C.-J., and Q. Xu, 1992: A simple adjoint method of wind analysis for single-Doppler data. *J. Atmos. Oceanic Technol.,* **9,** 588–598.

——, and ——, 1996: Least squares retrieval of microburst winds from single Doppler radar data. *Mon. Wea. Rev.,* **124,** 1132–1144.

Ray, P. S., C. L. Ziegler, and W. Bumgarner, 1980: Single- and multiple-Doppler radar observations of tornadic storms. *Mon. Wea. Rev.,* **108,** 1607–1625.

Roux, F., 1985: Retrieval of thermodynamic fields from multiple-Doppler radar data using the equations of motion and the thermodynamic equation. *Mon. Wea. Rev.,* **113,** 2142–2157.

——, 1988: The West African squall line observed on 23 June 1981 during COPT 81: Kinematics and thermodynamics of the convective region. *J. Atmos. Sci.,* **45,** 406–426.

——, and J. Sun, 1990: Single-Doppler observations of a West African squall line on 27–28 May 1981 during COPT 81: Kinematics, thermodynamics and water budget. *Mon. Wea. Rev.,* **118,** 1826–1854.

——, J. Testud, M. Payen, and B. Pinty, 1984: West African squall-line thermodynamic structure retrieved from dual-Doppler radar observations. *J. Atmos. Sci.,* **41,** 3104–3121.

——, V. Marecal, and D. Hauser, 1993: The 12/13 January 1998 narrow cold-frontal rainband observed during MFDP/FRONTS 87. Part I: Kinematics and thermodynamics. *J. Atmos. Sci.,* **50,** 951–974.

Sasaki, Y. K., P. S. Ray, J. S. Goerss, and P. Soliz, 1979: Inconsistent finite differencing errors in the variational adjustment of horizontal wind components. *J. Meteor. Soc. Japan,* **57,** 88–92.

Shapiro, A., S. Ellis, and J. Shaw, 1995: Single-Doppler velocity retrievals in the planetary boundary layer. *J. Atmos. Sci.,* **52,** 1265–1287.

Sun, J., and F. Roux, 1988: Thermodynamic structure of the trailing stratiform regions of two West African squall lines. *Ann. Geophys.,* **6,** 659–670.

——, and R. A. Houze Jr., 1992: Validation of a thermodynamic retrieval technique by application to a simulated squall line with trailing stratiform precipitation. *Mon. Wea. Rev.,* **120,** 1003–1018.

——, and N. A. Crook, 1996: Comparison of thermodynamic retrieval by the adjoint method with the traditional retrieval method. *Mon. Wea. Rev.,* **124,** 308–324.

——, D. W. Flicker, and D. K. Lilly, 1991: Recovery of three-dimensional wind and temperature fields from simulated Doppler radar data. *J. Atmos. Sci.,* **48,** 876–890.

Testud, J., and M. Chong, 1983: Three-dimensional wind field analysis from dual-Doppler radar data. Part I: Filtering, interpolating and differentiating the raw data. *J. Climate Appl. Meteor.,* **22,** 1204–1215.

Wurman, J., 1999: Preliminary results from the Radar Observations of Tornadoes and Thunderstorms Experiment (ROTATE-98/99). Preprints, *29th Int. Conf. on Radar Meteorology,* Montreal, Canada, Amer. Meteor. Soc., 613–616.

Xu, Q., C.-J. Qiu, and J.-X. Yu, 1994: Adjoint-method retrievals of low-altitude wind fields from single Doppler reflectivities measured during Phoenix II. *J. Atmos. Oceanic Technol.,* **11,** 275–288.

Zhang, J., and T. Gal-Chen, 1996: Single-Doppler wind retrieval in the moving frame of reference. *J. Atmos. Sci.,* **53,** 2609–2623.